RESEARCH ARTICLE

Improved Prostate Biparameter Magnetic Resonance Image Segmentation Based on Def-UNet

XUNAN HUANG[1], **BO PANG**[1], **TAO ZHANG**[1], **GUANG JIA**[2], **YING WANG**[1], **AND YONGLIN LI**[1]

[1]Air Traffic Control and Navigation College, Air Force Engineering University, Xi'an, Shannxi 710051, China
[2]School of Computer Science and Technology, Xidian University, Xi'an, Shannxi 710071, China

Corresponding authors: Ying Wang (karenjjj@163.com) and Yonglin Li (liyonglin1@126.com)

ABSTRACT The prostate tissue structure is complex, the shape and size change is relatively large, and the surrounding anatomical structure is complex, so the task of segmenting prostate and prostate cancer is somewhat challenging. In this paper, the idea of deformable convolution is combined with the U-net algorithm widely used in medical image segmentation. By using the deformable convolution module at a specific position in the ordinary U-Net network structure, additional offsets can be added to the convolution operator and the spatial sampling position can be changed by learning the offset of the target segmentation area. The fixed receptive field of the traditional convolution operator is shifted to an adaptive receptive field that can feel the change of features, and the segmentation accuracy of the target area is improved. Experiments show that the algorithm can improve the accuracy of prostate segmentation. In this paper, the segmentation model trained with healthy prostate data is transferred to the prostate cancer data set for secondary training by simulating the way doctors read pictures. Experiments show that the segmentation effect of the lesion area is significantly improved compared with the network model trained directly with small sample prostate cancer data. The research results can provide further exploration ideas for the application of medical domain knowledge in deep learning models.

INDEX TERMS Precision medicine, magnetic resonance imaging, medical image fusion, medical image segmentation, convolutional neural network.

I. INTRODUCTION

Since the 1980s, magnetic resonance imaging (MRI) has been used for noninvasive evaluation of the prostate and its surrounding structures [1]. Magnetic resonance imaging has proven to be the most accurate noninvasive method for detecting prostate cancer [2]. In recent years, due to the rapid development of deep neural networks, medical image analysis and computer-aided diagnosis (CAD) have made considerable progress [3]. Therefore, accurate prostate segmentation plays a vital role in many medical imaging and image analysis tasks, such as cancer detection, patient management, and treatment planning, including surgical planning [4], [5]. However, manual segmentation is a very time-consuming task [6]; in addition, it is subjective and based

The associate editor coordinating the review of this manuscript and approving it for publication was Jinhua Sheng.

on the level of experience, resulting in poor reproducibility and high interobserver variability [7]. If a computer-aided diagnosis can be used to accurately segment the prostate structures in images, it will help doctors diagnose and judge prostate diseases [7]. Therefore, reliable automatic segmentation of the prostate area is very valuable in daily clinical practice [6]. Automatic segmentation of the prostate from MR images is very challenging [8]. There are several reasons. First, the prostate is a small organ in males and usually only occupies a small part of the entire MR image [9]. Second, due to the accumulation of urine in the bladder or whether a rectal coil is used during imaging, the position of the prostate in images will also change [10], [11]. In addition, the background area occupies a large part of the input image volume and contains various complex objects. Due to the ambiguity of the boundary of the gland, it is difficult to distinguish it from the surrounding tissues, and the internal
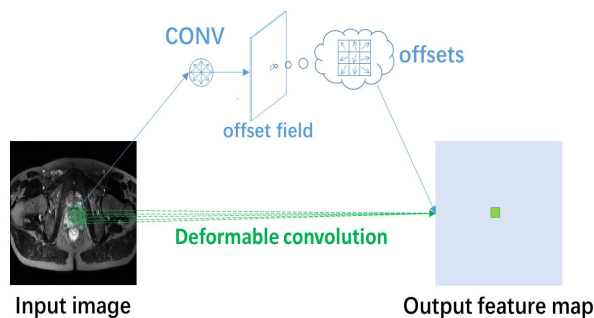
structure of the gland is quite different at different anatomical levels. Using different imaging protocols to examine different MR images can result in large differences in signal strength [12]. Finally, the morphology of the prostate tissue may change due to the stage and location of the tumor (e.g., in the PZ region, in the CZ region). In addition, the shape of the tumor is generally irregular, which is a challenge for the segmentation of the tumor area [13]. In clinical practice, multiparameter magnetic resonance images are often used for accurate prostate segmentation. Traditionally, prostate cancer is diagnosed with a biopsy [14]. However, there is evidence that multiparametric MRI scans can help locate the target area, thus reducing the number of unnecessary biopsies by half [15], minimizing the number of clinically meaningless prostate cancer diagnoses, and increasing the recognition of clinically significant prostate cancer [16]. The European Society of Urogenital Radiology (ESUR) has established the prostate imaging reporting and data system (PI-RADS) score for mpMRI. The T2W image on the transverse section is considered to be the best image to describe the prostate anatomical structure [17]. However, in many cases, T2W imaging cannot be used to reliably distinguish prostate cancer from prostate intraepithelial neoplasia, bleeding, postradiotherapy changes, or prostatitis [18], [19], [20]. In the ADC (Apparent diffusion coefficient) graph, a low ADC value means that diffusion is limited, while a high ADC value comes from tissues with relatively free diffusion. Since the cellularity of the tissue and the integrity of the cell membrane are inversely proportional to the diffusion of molecules in the tissue, the measurement of water diffusion provides information about the tissue structure in benign and malignant tissues [21], [22]. Studies have shown that the ADC of prostate cancer is lower than that of the surrounding healthy prostate tissue, and the ADC graph shows a low signal. Research by Xu et al. showed that bpMRI and mpMRI are comparable in detecting prostate cancer and identifying clinically significant lesions [23]. Kuhl et al. [24] surveyed 542 patients with PSA $\geq$ 3 ng/mL and negative transrectal ultrasound-guided biopsy results and showed that bpMRI and mpMRI had similar diagnostic accuracy for clinically significant tumors.

The focus of this paper is on the use of the latest deformable U-Net convolutional network structure to automatically segment the prostate from bpMR images, an important prerequisite for computer-aided design [25]. The division of the prostate area is of great significance for medical image analysis, but it is challenging due to the imbalance of the labeled data, background interference, and high anatomical variability. In this work, we propose a deformable U-Net convolutional network structure that uses the basic local features and U-shaped structure of the prostate to segment prostate MR images in an end-to-end manner. In recent years, a new deformable convolutional network [26], [27] has been proposed. Inspired by this, we integrate the deformable convolution into the proposed neural network, namely, Def-UNet, and use an upsampling operator to improve the output resolution. The purpose is to extract contextual information and achieve precise positioning by combining low-level feature mapping with high-level feature mapping. Def-UNet can capture prostate regions with different shapes and proportions through adaptive shapes. Experiments show that the accuracy and reliability of this method for automatic segmentation of prostate magnetic resonance images are better than those of the existing methods.

Automatic prostate segmentation methods and algorithms have always been a research hotspot. Before major breakthroughs in the field of deep learning, deformable atlas-based segmentation [28] and spatially continuous max-flow [29] models were proposed. In addition, some methods were based on primary machine learning, such as random forest, edge space learning [30], c-means clustering and zone morphology [31], and pattern recognition methods [32]. Among these methods, Martin et al. [33] combined a deformable model and a probabilistic atlas-based model to segment prostate MR images. The clustering method proposed by Zhang et al. separates the prostate from the surrounding tissues and then performs postprocessing through active contours. Chilali proposed a prostate and region segmentation method based on atlas and c-means clustering to segment the transitional and surrounding regions of the prostate [34].

Since their development, deep convolutional neural networks (CNNs) have played an increasingly important role as automatic segmentation methods in the field of medical image semantic segmentation. CNNs are based on hierarchical feature extraction. Compared with methods using manual features, CNNs have higher performance. Many studies have explored CNN-based medical image segmentation methods. Jia et al. [35] used coarse-to-fine segmentation. They also used atlas registration and pixel classification based on a CNN and finally proposed integrated learning for fine segmentation and achieved better results. Furthermore, Cheng et al. [36] proposed an overall nested network to segment the prostate and claimed that the Dice score is much higher than that of the patch-based CNN. Tian et al. [37] trained and tested a CNN called PSNet and segmented the prostate using three independent datasets. The method achieved a Dice score of 85.0±3.8% and satisfactory segmentation accuracy results. In CNN-based segmentation, small differences in the shape and appearance of the prostate are usually ignored. Therefore, Karimi et al. [38] proposed a CNN that incorporates a statistical shape model. The results show that compared with the normal CNN method, the proposed method has significant differences that achieve improved performance. Guo et al. [39] proposed a new hybrid model that combines the deep learning model and the deformable model and matches the features extracted by the deep learning model with the mask line in the label through the sparse matching method. The DSC of this method is 87.1%. In addition, U-net uses the skip connection operation to connect each pair of the down-sampling layer and the up-sampling layer, which makes the spatial information
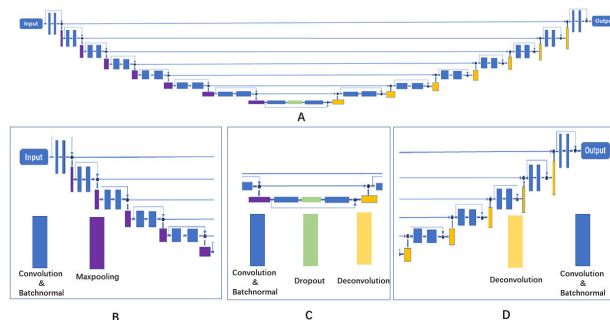
FIGURE 1. Schematic diagram of the deformation convolution operation on the prostate area.

FIGURE 2. Basic U-Net structure. Basic U-Net structure. (A) Overview of Convolution Neural Network Structure,(B) Downsampling part, (C) Bottom part, (D) Upsampling part.

directly applied to much deeper layers and a more accurate segmentation result [40]. Zhu et al [41]provided methods based on 3D volume space segmentation, and Millitari et al. [42] used 3D U-Net to segment the vestibular and transitional regions (the DSCs were 0.85 and 0.60, respectively). Zabihollahy et al. used two parallel U-Nets to segment the prostate and its area on T2W and ADC maps [43]. Zhu et al. [44] also provided methods to automatically segment the prostate using multiparameter MR images. Qian et al. designed a new method of prostate cancer detection based on MR images, which is recorded as ProCDet, experimental results show that the ProCDet can obtain competitive detection performance [45]. Qian et al proposed a new prostate segmentation network based on MR images, denoted as ProSegNet, which integrated the spatial attention mechanism and the channel attention mechanism to focus on the important features while ignoring the invalid features [46].

Inspired by the above work, we explore a U-Net with deformable operations, namely, Def-UNet, as a neural network structure that can effectively handle the large anatomical variability of the prostate through a deformable convolution block.

II. THE PROPOSED ALGORITHM
To better utilize the performance of deformable convolution, three different network deformable convolution architecture tests are designed to determine the most effective deformable convolution network model, and the selected image preprocessing technology is used to form the best possible training framework. The Dice coefficient, average relative absolute volume difference, average Hausdorff distance, and average surface distance of symmetrical positions are used as evaluation indicators to verify and test the segmentation mask and compare it with other state-of-the-art methods. Our goal is to establish a new segmentation method for prostate magnetic resonance images based on deep learning. Because the deep neural network that is used is easily affected by the complex and changeable background regions that account for a large part of the input image volume, the segmentation accuracy of the prostate region is often low. We use a cascaded multi-level U-Net model. In this model, the original convolution

filter is used in the first convolution layer of the model, and a deformed convolution layer is added to the subsequent four convolution layers for segmentation and refinement. The advantages of the proposed unit and deformable network are described in the following subsections. It is expected that the prostate segmentation accuracy will be improved by adding a deformable convolution block. To explore how deformable convolution blocks improve the segmentation effect, deformable convolution blocks are added to the U-Net network in three structure modes to conduct experiments, and the results are analyzed.

A. OVERALL NETWORK MODEL
We propose the Def-UNet network structure based on the basic U-Net structure. The basic U-Net network structure diagram of this architecture is shown in Figure 2. The network is composed of a downsampling part, a bottom part, and a upsampling part.

Seven basic convolution blocks are set in the downsampling part, and seven basic convolution blocks with the same structure are set in the upsampling part. At the bottom of the U-shaped network structure, a special convolution block connects the downsampling part on the left and the upsampling part on the right.

In the downsampling part, as shown in Figure 2, the input image is guided to the first basic block, and then the output feature map (convolution output) of the first basic block is fed as the input to the next basic block. This process is repeated seven times in the seven basic convolutional blocks. After each basic block of the downsampling part, the maximum convolution pooling operation [47] is used to reduce the size of the feature map by half.

At the bottom of the U-shaped structure, there is a special block connecting the downsampling and upsampling parts. In the upsampling part, there is a deconvolution layer (3×3 convolution with a step size of 2). After the feature map is deconvolved, the size of the image is doubled, and then a basic convolution block is connected. The final segmented image output by the network has the same size as the input

image (256 × 256). Since multiple convolutional layers and maximum pooling layers are continuously used in the downsampling process, the spatial information of some images is lost, which in turn causes more information to be lost in the feature maps of the subsequent upsampling part. To improve the quality of the upsampling part of the feature map, a long connection is used to extract the data from the downsampling part and copy it to the upsampling part to participate in the calculation to improve the quality of the upsampling feature map. In the architecture proposed in this paper, each of the seven basic convolutional blocks uses seven long connections to copy the extracted feature maps to the upsampling part and connect them with the deconvolved feature maps.
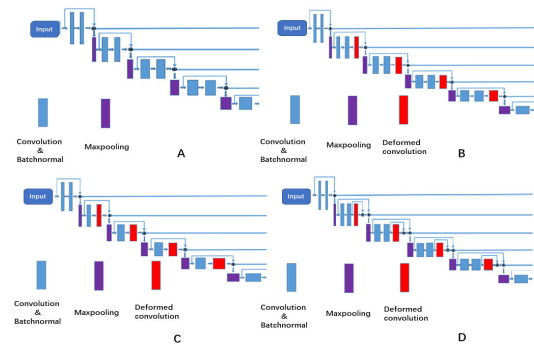
B. BASIC CONVOLUTION STRUCTURE

Each basic convolution block contains two convolution operation layers and two batch normalization layers. The purpose of BN (Batch Normalization) is to normalize the output of the network layer during training, and this normalization can speed up the training of the network [48].

A small 3 × 3 convolution filter is used in each convolution layer. By using a small convolution kernel, the network will apply more nonlinear layers, which can reduce the number of model parameters. The BN layer is used after each convolution operation layer, and relu is used as the activation function during the convolution operation. The special convolution block is used at the bottom of the U-shaped structure. The difference between this block and the general convolution block is that after the first convolution and BN operation, a dropout layer is added. Dropout is an effective method that can eliminate complexity. The training data of the common adaptation can also be used for regularization. Dropout randomly deletes some features by omitting hidden layer units with a specified probability. Here, we set the dropout operation at the bottom of the U-shaped structure to control overfitting.

In each basic convolution block, we use the shortcut connection proposed by He. et al [49]. The shortcut connection allows the connection operator to combine the input feature map of the block with its output. This bypass connection directly connects the current block. The input is provided to the next block. In the last layer of our proposed network, we apply the sigmoid function [50] as a nonlinear output function. A sigmoid function is usually used for 2-classification tasks. Our final segmented image is a 2-classification result. The black part is the background, and the white part is the detected prostate cancer area.

C. DEFORMABLE CONVOLUTION STRUCTURE

In conventional convolutional layers, for a set network structure, the convolution size does not change, so the receptive field does not change. However, it is not ideal to use the same receptive field for different sized objects. In the field of target segmentation of medical images, the lesion area to be segmented usually has an irregular shape and size.

FIGURE 3. Schematic diagram of the deformable convolutional network structure. (A) Basic U-Net structure, (B) Def-UNet1 structure, (C) Def-UNet2 structure, and (D) Def-UNet3 structure.

Based on previous experience, target segmentation can only be performed by increasing the depth of the network or using image enhancement algorithms, and the image is sent to the network. Rotational scaling allows the neural network to increase its tolerance to image irregularities. However, even though this cannot solve the large deformation problem in the object space well and simultaneously increases the training difficulty and training time, we add the deformable convolution module to the classic medical image U-Net segmentation network to obtain more accurate segmentation results.

In the basic U-Net model, we add the deformable convolution to different parts of the network to find the structure with the best effect. Because the first downsampled convolution block is used to extract the basic features of the image, the experiments prove that after adding the deformable convolution to the first downsampled convolution block, the network training time will become very long, but the training result will not greatly improve. In addition, after multiple convolution and downsampling operations, the size of the feature map becomes very small, the feature information is abstracted, and the meaning of using the deformable convolution is not obvious. Therefore, considering the above two factors comprehensively, a deformable convolution operation is added to the basic convolution block of the second, third, fourth, and fifth layers. After confirming the approximate location where the deformed convolution should be added, we design 3 ways to add the deformed convolution layer.

Def-UNet1 does not change the original convolution based on the conventional U-Net but adds a deformed convolution layer after performing two convolution operations in each general convolution block. The Def-UNet2 structure makes certain changes to the original convolution based on the conventional U-Net. In each general convolution block, the second convolution layer is directly replaced with a deformed convolution, and the resulting feature map and convolution are the input connections of the block. Def-UNet3 is based on the Def-UNet1 model. The shortcut connections mentioned above are added before and after the deformable convolutional layer.

III. EXPERIMENTAL MATERIALS AND METHODS

A. DESCRIPTION OF THE EXPERIMENTAL DATASET

The data set used in this study is divided into two parts, one is the healthy prostate data set, and the other is the prostate tumor data set.

In this study, network pre-training is conducted on the healthy prostate segmentation dataset named PROMISE12. The dataset was divided into two parts: a training set and a test set. The training set contained 50 healthy volunteers' T2W sequence magnetic resonance imaging data collected by radiologists. The ground truth of the prostate area was outlined, and the magnetic resonance imaging of each patient contained approximately 20–40 pictures. The data of these volunteers come from the magnetic resonance equipment of different hospitals. Therefore, the data vary in terms of voxel size, dynamic range, position, and field of view, and there were different collection protocols and differences in anatomical appearances. The test set part contained the MR image data of 30 patients. Each patient had 63 T2W sequence magnetic resonance images, and the ground truths of the prostate areas were outlined by the radiologist.

MRI data of prostate tumor downloaded from I2CVB (http://i2cvb.github.io/#prostate-data). There were 19 patients in the prostate cancer magnetic resonance dataset: 17 were confirmed to have prostate cancer (CaP) by biopsy, and 2 had a negative biopsy. Of the above 17 patients, 12 had CaP in the peripheral zone (PZ), 3 had CaP in the central gland (CG), and 2 had aggressive CaP in the PZ and CG zones. An experienced radiologist segmented the prostate and prostate cancer areas on the images. We randomly selected images from 13 of the 17 prostate cancer patients as the training set and the remaining patients' images as the test set.

B. DATA PREPROCESSING

The scanned images of the PROMISE12 dataset were provided in raw 3D image format. We processed the dataset into many axial two-dimensional images. The image size was adjusted to 256×256. Due to the large grayscale range of the images in the dataset, to facilitate the training of this experiment, the medical images in DICOM format were converted into 256 grayscale images (pixel value 0–255) and input to the network for training. Due to the large number of images in the PROMISE12 dataset, the following strategies were used to enhance the images: random rotation from 0 to 10 degrees, random movement along the x-axis and y-axis at one-tenth of the corresponding image size, random zooming by a factor ranging from 1 to 1.2, and random horizontal or vertical rotation.

C. TRAINING PARAMETER SETTINGS

In our experiments, the training and testing of the model were implemented using the Python language. All experiments were performed on a Windows workstation equipped with 16 GB of memory, an Intel Core i5 7500 CPU and an NVIDIA GTX1060 graphics card with 6 GB of video
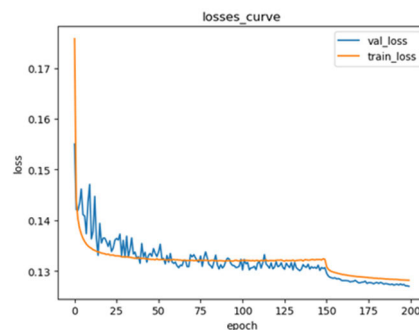

FIGURE 4. The plot of network model training loss and validation set loss.

memory. The training time of the CNN model was 40 h, and it was accelerated by CuDNN. The network parameters were randomly initialized, Adma optimizer was used, and the method of adjusting the learning rate was adopted. The initial learning rate was 0.001, and the learning rate was reduced to 0.0001 at 150 epoch. A total of 200 epoch was trained. The weight of each convolution block structure in the network was initialized randomly. The batch size was set to 16.

In the training process of the network structure, the healthy prostate images were used as the input images, and the stochastic gradient descent algorithm was used to update the weights. Keras and TensorFlow backends were used to implement the proposed method. We used the same training set to train the three deformable convolutional network structures and all comparison algorithms. During the training process, each epoch was verified using the validation set. After all training was completed, the test set was sent to the trained network for testing, and the test results were summarized.

In the training of this model, Dice_loss is adopted as the loss function, which is defined as:

$$
\text{Dice\_loss} = \log \left(\frac{\sum\limits_{n=1}^{N} p_n r_n + \varepsilon}{\sum\limits_{n=1}^{N} p_n + r_n + \varepsilon} + \frac{\sum\limits_{n=1}^{N} (1 - p_n)(1 - r_n) + \varepsilon}{\sum\limits_{n=1}^{N} 2 - p_n - r_n + \varepsilon} \right) \quad (1)
$$

where p_n represents the nth predicted value, r_n represents the corresponding true value, N is the number of all pixels, and ε =1e-15 is a constant. The model is validated by the validation set in each epoch. If the val_loss embodied in the validation set is low, the model parameters are retained.

Figure 4 shows the plot of the initial learning rate of 0.01 and the training loss function using 0.001 as the learning rate at 150 epochs, where the blue curve represents the validation set loss and the green curve represents the training set loss. It is observed from the graph that both the validation set loss and the training set loss decrease significantly during the training process. The accuracy of the network training can meet the requirements when the network is trained for 200 epochs, and the training/validation loss is less than 0.13.
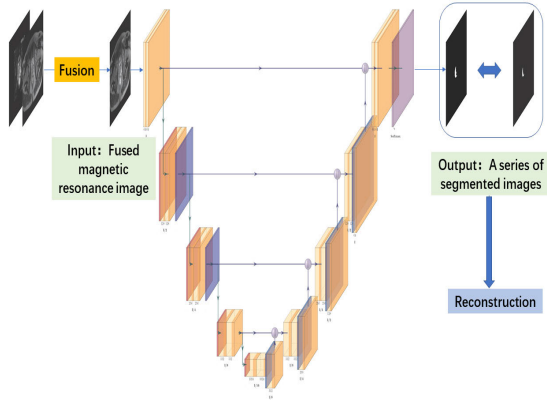
FIGURE 5. Flowchart of the segmentation and reconstruction of magnetic resonance images after fusion.

D. SEGMENTATION AND RECONSTRUCTION OF MAGNETIC RESONANCE IMAGES AFTER FUSION

In this study, a multiparameter magnetic resonance image prostate cancer segmentation framework based on U-Net was proposed. First, the Laplacian pyramid was used to fuse the multiparameter magnetic resonance images into grayscale images, and then the fused grayscale images were sent to U-Net for training. The training network used the trained model in Section III-C and the transfer learning method to continue training on prostate cancer images. After all training was completed, the prostate cancer test set was tested, and the test results were summarized. Figure 5 shows that the entire process is mainly divided into three steps: fusion, segmentation, and reconstruction. Specifically, in the fusion step, the medical image fusion algorithm [51] was used to fuse T2W and ADC sequence images into one image, and convolutional neural network model training was used to extract features from T2W and ADC sequence magnetic resonance images. Then, the effective aggregation weight to fuse these representations was predicted through the network. Different types of magnetic resonance data were fused for downstream tasks, and the extraction of effective information from the multiparameter images was completed. The deformable convolutional neural network structure proposed in this chapter was used to segment the fused images. The combined fused dual-parameter magnetic resonance images could be used as deep learning inputs. The image segmentation network designed for the prostate area will be output to detect cancer in images. As a result, the cancer tissue was segmented and labeled. The entire process is shown in Figure 5. The output result is binary images. The area with a pixel value of 1 (the white part in the figure) represents the prostate cancer area, and the area with a pixel value of 0 (the black part in the figure) represents no prostate cancer tissue as background.

E. OBJECTIVE EVALUATION INDICES

In this experiment, the DSC, RVD, ASD, H-distance and other indicators were used to evaluate the image segmentation results.

The basic evaluation standard of the Dice similarity coefficient (DSC), which is commonly used in the segmentation process, is a measure of ensemble similarity. The best value is 1, and the worst value is 0. The formula is as follows:

$$DSC = \frac{2\,|S_A \cap S_B|}{|S_A| + |S_B|} \tag{2}$$

where $|S_A|$ is the number of prostate target pixels from the manual segmentation of the ground truth, and $|S_B|$ is the number of prostate pixels in the segmentation result of the proposed method.

The calculation method of the absolute volume difference divides the total volume of the segmented prostate image mask by the real volume of the ground truth. Then, 1 is subtracted from this number, and the result is multiplied by 100 to express the result as a percentage:

$$RVD = \left(\frac{|S_A| - |S_B|}{|S_B|}\right) \times 100 \tag{3}$$

The Hausdorff distance is a measure that describes the degree of similarity between two sets of points. It defines the distance between two sets of points. Suppose there are two sets of A and B. The Hausdorff distance between sets of points is defined as:

$$h(A, B) = \max(a \in A)\{\min(b \in B)\,\|a - b\|\} \tag{4}$$

$$h(B, A) = \max(b \in B)\{\min(a \in A)\,\|b - a\|\} \tag{5}$$

$$H(A, B) = \max(h(A, B), h(B, A)) \tag{6}$$

Here, the maximum distance $||a_i - b_j||$, from each point a_i in point set A to point b_j in set B closest to this point are sorted and represented as h(A, B). The meaning of the value of h(A, B) is similar to that of h(B, A). The bidirectional Hausdorff distance H(A, B) is the maximum of the unidirectional distances h(A, B) and h(B,A). It measures the maximum degree of mismatch between the manually segmented ground truth and the prostate region in the segmentation result.

The average symmetric surface distance (ASD) is given as:

$$ASD = \frac{\left(\sum_{a \in S_A, b \in S_B} \min \|a - b\| + \sum_{a \in S_A, b \in S_B} \min \|b - a\|\right)}{|S_A| + |S_B|} \tag{7}$$

IV. RESULTS

A. RESULTS OF PROSTATE SEGMENTATION

To evaluate the performance of the three models we designed, we compared our method with the most common segmentation methods. We chose U-Net [28], Dense U-Net [52], 3D-FCN [53], 3D-VNet [54], Attention U-Net [55], and the GAN [56]. For a fair comparison, all the methods were reproduced. Through visual comparison with manual segmentation contours, the performance of the proposed deep learning method was qualitatively evaluated. Figure 6 shows the predicted segmentation results. Several representative photos are selected in the results. We compared U-Net, 3D-V-Net, 3D-FCN and attention U-Net. Compared with the traditional segmentation model, the performance is significantly
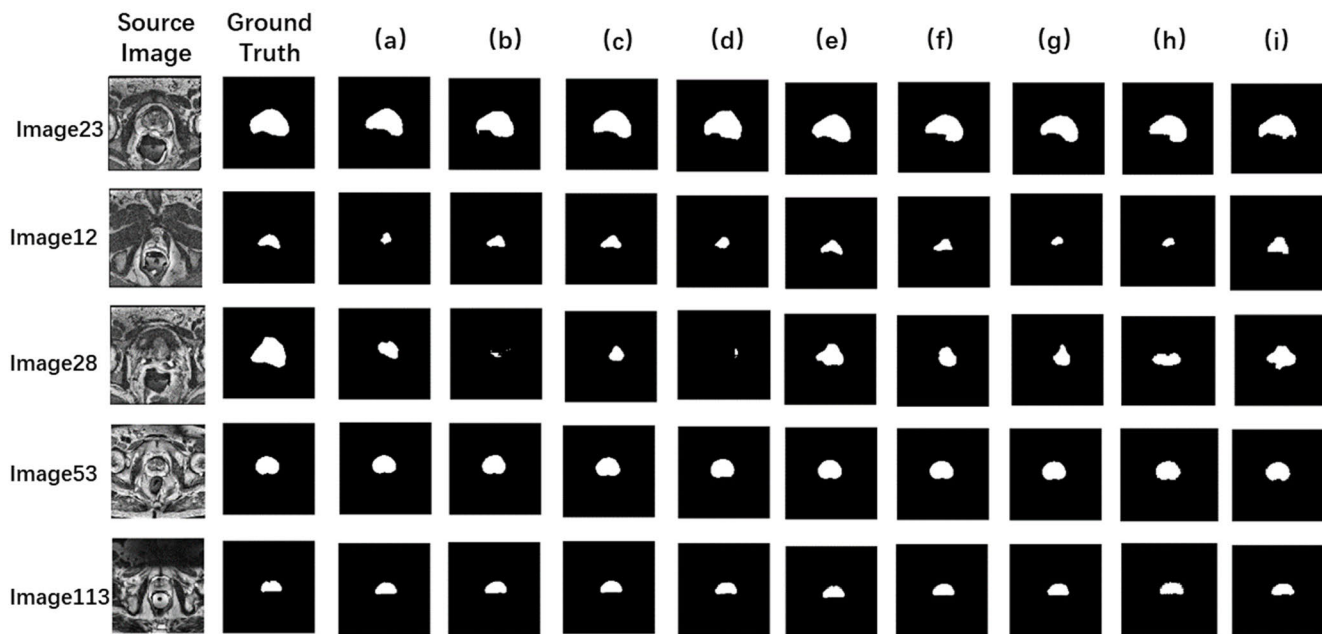
FIGURE 6. Comparison of prostate segmentation results. (a) U-Net (b) Dense U-Net (c) 3D-FCN (d) 3D-VNet (e) Attention U-Net (f) GAN.(g) ef-Unet1 (h) Def-Unet2 (i) Def-Unet3.

TABLE 1. Objective evaluation results of prostate segmentation.

	U-Net[43]	Dense U-Net[54]	3d-FCN[55]	3d-VNet[55]	Attention U-Net[53]	GAN[53]	Def-Unet1	Def-Unet2	Def-Unet3
Accuracy	0.8309	0.8472	0.8380	0.8392	0.8522	0.868	**0.8782**	0.8416	0.8566
Mean Vol DSC	0.7486	0.8579	0.8494	0.8482	0.8509	0.8709	**0.8734**	0.8501	0.8652
Media DSC	0.7398	0.8594	0.8539	0.8359	0.8604	0.8588	**0.8844**	0.8533	0.8808
Std DSC	0.0330	0.056	0.058	0.0489	0.0318	0.0384	**0.0314**	0.0480	0.0631
Recall	0.8114	0.8119	0.7974	0.7964	0.8218	0.8307	**0.8799**	0.7981	0.8134
Mean MSD	2.7997	1.8051	1.8943	1.9818	2.1359	1.5321	**1.4869**	1.99	1.548
Mean Abs	23.5985	16.535	20.0254	19.644	19.5294	16.4996	15.6057	19.22	**13.941**
Precision	0.8514	0.8857	0.8830	0.8856	0.8850	0.8769	**0.9088**	0.8901	0.9044
Mean Hass Dist	26.316	24.3364	24.961	15.431	13.7946	**10.3492**	10.9443	13.256	12.946

improved when using our model. This method can obtain more accurate partition boundaries and shapes.

Overall, after adding the deformation convolution, the accuracy of prostate region segmentation is improved. For example, in Img23, the contour size and shape of the prostate region segmented by the Def-UNet1 model in this article are the most similar to those of the ground truth. In the Def-UNet2 and Def-UNet3 models, the lower right parts of the image are quite different from the ground truth. In summary, Img23 contains an irregularly shaped area that is difficult to segment. The contour of the prostate area of the tumor

area segmented by the Def-UNet1 model is roughly the same as the ground truth, but the size is reduced.

The Def-UNet2 and Def-UNet3 models can segment a relatively small area, but the contour shape is quite different from the ground truth. The prostate area in Img12 is a small irregular triangle-like area. Our Def-UNet1, Def-UNet2 and Def-UNet3 models all segment a triangle-like region. In Img113, the prostate area is a semicircular area with a defect in the upper part. All comparison methods can segment the prostate area better, but the Def-UNet1 method in this article is more refined, and the upper defect can also be

TABLE 2. Objective evaluation results of prostate cancer region segmentation.

	T2W	ADC	Fused image
Accuracy	0.5969	0.8205	0.9189
Mean Vol DSC	0.5877	0.8107	0.9213
Media DSC	0.6016	0.8279	0.9115
Std DSC	0.0622	0.0516	0.0426
Recall	0.5269	0.7936	0.8928
Mean MSD	1.9253	1.6426	1.5549
Mean Abs	19.6265	17.0036	16.5462
Precision	0.7529	0.8679	0.9314
Mean Hass Dist	18.9439	14.6954	13.7695
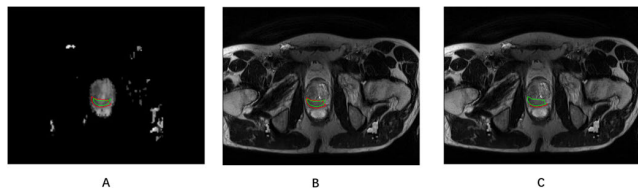
FIGURE 7. Schematic diagram of the segmentation results of the same anatomical structure of patient 3 with ADC sequence image (A), T2W image (B), and fusion image (C). The red outline in the figure is the boundary of the groundtruth area marked by the doctor, and the green outline is the boundary of the results of the segmented prostate tumor area.
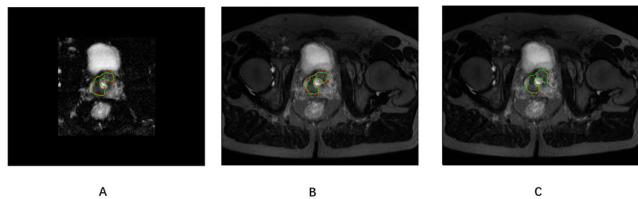
FIGURE 8. Schematic diagram of the segmentation results of the same anatomical structure of patient 4 with ADC sequence image (A), T2W image (B), and fusion image (C).

segmented well. The prostate area in Img53 is a regular circular area. Almost all comparison methods can segment the lesion area very well. In summary, this experiment proves that in irregular prostate region segmentation, only the detection result of our method is close to the real situation of the ground truth.

The proposed method can be used because we have added deformation convolution to better perceive the irregularity of the region. The contour of the segmented prostate area is more accurate and closer to the irregular boundary drawn by the ground truth. These results can explain and promote the use of the convolutional neural network to more accurately identify the prostate cancer area.

The detailed comparison results of the objective evaluation indicators are shown in Table 1. The results show that our proposed model can achieve better results, especially in terms of accuracy, precision and DSC, compared with current mainstream prostate segmentation methods.

FIGURE 9. A three-dimensional reconstruction of the segmented prostate cancer region in patient 6.

Under similar conditions, the average DSC result of our model on the validation set can reach 87.34, which is significantly better than those of other advanced methods. As shown in the table, the proposed Def-UNet1 achieves the maximum values in terms of the accuracy and Dice coefficient. Regarding the degree, although the Mean Hass Dist is not the best result, it is close to the optimal value, which also explains why the GAN method can learn more spatial edge information through the 3-dimensional space. Furthermore, Def-UNet3 can better improve the performance regarding the absolute volume difference compared with the proposed Def-UNet1.

B. SEGMENTATION AND RECONSTRUCTION RESULTS OF PROSTATE CANCER

In order to improve the segmentation accuracy of prostate cancer regions, this paper proposes to fuse magnetic resonance images of T2W sequences and ADC sequences as shown in Figure 5, and then send these fusion images as input into Def-Unet network after pretraining in promise12 prostate magnetic resonance image data set for retraining. In addition, the Def-Unet convolutional neural network structure after pre-training was used to train the separate T2W and ADC sequence images respectively, and the segmentation results were compared with the fusion image segmentation, so as to explore whether the fusion magnetic resonance image as the input can achieve a higher segmentation accuracy than the single sequence image training. Figure 7 shows the results of prostate cancer segmentation for patient 3.

The red frame represents the ground truth boundary marked by the radiologist, and the green part is the boundary of the prostate cancer region segmented by the deep learning algorithm. The overall segmentation effect of the three different images is acceptable, and the convolutional neural network can achieve a good effect through training and learning. The difference between the green edge and the red edge is not large, but the segmentation effect of the fusion image shown in Figure 7C is the best.

Figure 8 shows the results of prostate cancer segmentation for patient 4. The figure shows that the overall segmentation effect is not as good as that of patient 3. The boundary of the green segmentation area is smaller than the boundary of the red ground truth, and the fusion image in 8C improves the segmentation accuracy of the prostate cancer area.

In these steps, T2W, ADC, and their fusion images were trained once, and their respective DSC averages were calculated. The three groups of neural networks were trained to obtain the average DSC. Table 2 shows that the fusion and U-Net network training designed in the article has a good segmentation effect for prostate cancer. The segmentation accuracy of the prostate tumor for the T2W sequence is only 0.5969, and the segmentation accuracy of the ADC sequence is approximately 0.8205. The segmentation accuracy using fusion images can be improved to approximately 0.92.

After obtaining the segmentation results of the prostate cancer area, the layer thickness information in the original MRI DICOM file (i.e., the sampling interval between the two images) was read, and then the medical image three-dimensional reconstruction software (AIMIS3D software is developed by Xi'an Key Laboratory of Big Data and Visual Intelligence Technology, Xidian University. The software download website is www.cvnis.net/caimi/) was used to reconstruct the segmentation results, and the three-dimensional structure of the prostate was generated. The model can be rotated, zoomed, and measured arbitrarily in the software, and the model can also be generated into an STL file for 3D printing of the physical model.

V. DISCUSSION

Generally, U-Net includes batch normalization and cascading. When processing image details by deepening the network structure, more accurate segmentation results are expected to be produced. With the development of technology, some image segmentation algorithms based on three-dimensional space, such as 3D-VNet and 3D-FCN, were introduced. It is expected that more accurate segmentation in three-dimensional space can be obtained through learning the three-dimensional space, but this will increase the amount of data and the training time. In recent years, some strategically improved algorithms for U-Net segmentation, such as adding an attention mechanism, were also proposed. The attention mechanism in deep learning focuses the attention of the network on important or key points in the U-Net segmentation process while ignoring other unimportant points and information to improve segmentation accuracy. By using the idea of a deformable convolutional network, the traditional U-Net network can achieve a better segmentation effect by training two-dimensional images, which is even better than that of the segmentation algorithm based on three-dimensional image training. The possible reason is the training of three-dimensional images, which requires a longer training time and more training image data. In this work, we propose a novel network architecture inspired by U-Net and a deformable convolutional network. We propose a fixed-point deformable U-Net network (Def-UNet) to address the problem of the large variability in the anatomical structure of the prostate and improve the selection of the location of feature pixels in U-Net. Our method combines the advantages of these two networks to segment the prostate and its regions. Def-UNet appropriately offsets the sampling position of the standard filter in the convolution based on the deformed convolution, which makes the sampling grid more effective for the irregular area of the prostate. The offset is obtained from the input image through an additional convolutional layer. Deformable U-Net can handle spatial transformation in a simple and effective approach and improve the geometric transformation modeling ability of U-Net.

Judging from the visual effect of the results of prostate cancer segmentation, the segmentation effect of the prostate cancer area in Figure 8 is better because its staging is relatively late and the tumor tissue is relatively large. Regardless of whether an ADC image or T2W image is used, the tumor area shows a low signal and is significantly different from the surrounding normal tissues. For this type of tumor area with obvious characteristics, a single MRI sequence can be used to achieve a good segmentation effect, but the use of fusion will improve the accuracy of the edge of the segmented area of the image. In Figure 7, the tumor is located in the area between the prostate and the rectum. There are more complex features in the prostate and rectum regions of the image. Moreover, the tumor has irregular edges and is not as large as that in Figure 8. This is an accurate segmentation of the tumor and brings a certain challenge. The prostate tumor regions segmented in T2W and ADC images were both smaller than the ground truth. It may be that the junction between the tumor and normal tissue is not obvious, and the deep learning network has not extracted suitable feature information. Using the fusion image for segmentation is equivalent to extracting and fusing the useful information of the two images, which can enable the network to obtain better features during the training process. The segmentation results show that compared to the separate T2W sequence or ADC sequence, the segmentation performed after fusion greatly improved the results, but the overall segmentation area was still smaller than the ground truth. Figure 7 shows that the segmentation effect near the rectum is not good. In general, the segmentation accuracy of prostate cancer using the fused image will be greater than that of a separate sequence of magnetic resonance images in the segmentation of small tumors. In addition, compared with the normal prostate tissue area, the prostate tumor area has a more complex anatomical structure, more variable position, and more irregular shape. Therefore, compared with prostate segmentation in the objective evaluation standard results of image segmentation, the overall average prostate tumor segmentation score is lower than the healthy prostate tissue segmentation score.

The research in this article also has some limitations. To make this method more universal and robust, the method needs to be further verified in multicenter MR image experiments with different anatomical regions, image resolutions or image quality. It is expected that a more robust segmentation network of prostate cancer lesion areas will be developed. Another limitation is that the research in this article mainly focuses on a single T2W and ADC sequence MR image, and the current use of multiparameter MR sequence images to diagnose prostate cancer has become increasingly common.

In the future, we will seek to train effective prostate cancer segmentation algorithms using different sequences, such as DCE sequences and MRSI sequences. In future research, the participation of clinicians will also be considered, and targeted improvements will be made to the image segmentation algorithm under the guidance of urologists.

VI. CONCLUSION

Inspired by the current popular deep learning models, three Def-UNet models, which are U-Net-based MRI prostate segmentation network structures, were proposed. After training and cross-validation on the PROMISE12 training dataset, we selected an optimal Def-UNet model and implemented prostate segmentation based on the combination of the conventional U-Net and a convolutional deformation network on the PROMISE12 training dataset to form a new technology. The experimental results proved that the use of the deformable convolution can improve the performance of U-Net and achieve a good prostate MRI segmentation effect. The above algorithm was also used to segment prostate cancer images. A convolutional neural network was applied to the multiparameter magnetic resonance images to normalize the images using a normalization method. The fused images were used as the input of the training and sent to Def-UNet for training, and the test set images were used for testing. The experimental results showed that this method can effectively segment the prostate cancer area from MR images. The self-designed three-dimensional reconstruction software reconstructed the two-dimensional prostate segmentation results into a three-dimensional model and visually displayed the structure of the tumor area.

REFERENCES

[1] A. R. Padhani, "Dynamic contrast-enhanced MRI in clinical oncology: Current status and future directions," *J. Magn. Reson. Imag.*, vol. 16, no. 4, pp. 407–422, Oct. 2002, doi: 10.1002/jmri.10176.

[2] Y. Yuan, "Prostate cancer classification with multiparametric MRI transfer learning model," *Med. Phys.*, vol. 46, no. 2, pp. 756–765, 2018, doi: 10.1002/mp.13367.

[3] M. H. Le, J. Chen, L. Wang, Z. Wang, W. Liu, K.-T. Cheng, and X. Yang, "Automated diagnosis of prostate cancer in multi-parametric MRI based on multimodal convolutional neural networks," *Phys. Med. Biol.*, vol. 62, no. 16, pp. 6497–6514, Jul. 2017, doi: 10.1088/1361-6560/aa7731.

[4] B. Fei, "Computer-aided diagnosis of prostate cancer with MRI," *Current Opinion Biomed. Eng.*, vol. 3, pp. 20–27, Sep. 2017, doi: 10.1016/j.cobme.2017.09.009.

[5] G. Lemaître, R. Martí, J. Freixenet, J. C. Vilanova, P. M. Walker, and F. Meriaudeau, "Computer-aided detection and diagnosis for prostate cancer based on mono and multi-parametric MRI: A review," *Comput. Biol. Med.*, vol. 60, pp. 8–31, May 2015, doi: 10.1016/j.compbiomed.2015.02.009.

[6] J. Bleker, T. C. Kwee, D. Rouw, C. Roest, J. Borstlap, I. J. de Jong, R. A. J. O. Dierckx, H. Huisman, and D. Yakar, "A deep learning masked segmentation alternative to manual segmentation in biparametric MRI prostate cancer radiomics," *Eur. Radiol.*, vol. 32, no. 9, pp. 6526–6535, Apr. 2022, doi: 10.1007/s00330-022-08712-8.

[7] G. Salvaggio, A. Comelli, M. Portoghese, G. Cutaia, R. Cannella, F. Vernuccio, A. Stefano, N. Dispensa, G. La Tona, L. Salvaggio, M. Calamia, C. Gagliardo, R. Lagalla, and M. Midiri, "Deep learning network for segmentation of the prostate gland with median lobe enlargement in T2-weighted MR images: Comparison with manual segmentation method," *Current Problems Diagnostic Radiol.*, vol. 51, no. 3, pp. 328–333, May 2022, doi: 10.1067/j.cpradiol.2021.06.006.

[8] Z. Khan, N. Yahya, K. Alsaih, M. I. Al-Hiyali, and F. Meriaudeau, "Recent automatic segmentation algorithms of MRI prostate regions: A review," *IEEE Access*, vol. 9, pp. 97878–97905, 2021, doi: 10.1109/ACCESS.2021.3090825.

[9] H. Grönberg, *A Small Organ With a Vital Function*, vol. 358. Lancet, p. S55, doi: 10.1016/S0140-6736(01)07067-2.

[10] Y. M. Shlyapnikov, E. A. Malakhova, A. Z. Vinarov, N. V. Potoldykova, V. I. Vladimirov, E. Y. Zernii, A. A. Zamyatnin, and E. A. Shlyapnikova, "Cancer-retina antigens in the urine of bladder and prostate cancer patients," *Biochemistry Biokhimiia*, vol. 87, no. 11, pp. 1268–1276, Nov. 2022, doi: 10.1134/S0006297922110062.

[11] A. B. Porcaro, A. Borsato, M. Romano, T. Sava, C. Ghimenton, F. Migliorini, C. Monaco, E. Rubilotta, S. Z. Antoniolli, V. Lacola, and S. Montemezzi, "Accuracy of preoperative endo-rectal coil magnetic resonance imaging in detecting clinical under-staging of localized prostate cancer," *World J. Urology*, vol. 31, no. 5, pp. 1245–1251, Oct. 2013, doi: 10.1007/s00345-012-0900-7.

[12] R. Kalantar, G. Lin, J. M. Winfield, C. Messiou, S. Lalondrelle, M. D. Blackledge, and D.-M. Koh, "Automatic segmentation of pelvic cancers using deep learning: State-of-the-art approaches and challenges," *Diagnostics*, vol. 11, no. 11, p. 1964, Oct. 2021, doi: 10.3390/diagnostics11111964.

[13] M. Stone, K. Stone, and D. Paulson, "Scanning electron microscopy of hyperplastic and neoplastic human prostate," *Urological Res.*, vol. 4, no. 2, pp. 71–75, 1976, doi: 10.1007/bf00256320.

[14] D. Deniffel, G. M. Healy, X. Dong, S. Ghai, E. Salinas-Miranda, N. Fleshner, R. Hamilton, G. Kulkarni, A. Toi, T. van der Kwast, A. Zlotta, A. Finelli, N. Perlis, and M. A. Haider, "Avoiding unnecessary biopsy: MRI-based risk models versus a PI-RADS and PSA density strategy for clinically significant prostate cancer," *Radiology*, vol. 300, no. 2, pp. 369–379, Aug. 2021, doi: 10.1148/radiol.2021204112.

[15] E. Day, S. Nalagatla, J. S. Shin, B. Nair, M. Gurun, B. Meddings, G. McLaughlin, D. Chanock, and R. Clark, "Triaging patients to primary biopsy or prostate MRI based on digital rectal examination improves the detection rate of TRUS biopsy and avoids unnecessary biopsies," *J. Clin. Urology*, vol. 12, no. 2, pp. 117–121, Mar. 2019, doi: 10.1177/2051415818773965.

[16] A. E.-S. Bosaily, C. Parker, L. C. Brown, R. Gabe, R. G. Hindley, R. Kaplan, M. Emberton, and H. U. Ahmed, "PROMIS—Prostate MR imaging study: A paired validating cohort study evaluating the role of multi-parametric MRI in men with clinical suspicion of prostate cancer," *Contemp. Clin. Trials*, vol. 42, pp. 26–40, May 2015, doi: 10.1016/j.cct.2015.02.008.

[17] V. Kumar, G. S. Bora, R. Kumar, and N. R. Jagannathan, "Multiparametric (MP) MRI of prostate cancer," *Prog. Nucl. Magn. Reson. Spectrosc.*, vol. 105, pp. 23–40, Apr. 2018, doi: 10.1016/j.pnmrs.2018.01.001.

[18] A. P. S. Kirkham, M. Emberton, and C. Allen, "How good is MRI at detecting and characterising cancer within the prostate?" *Eur. Urology*, vol. 50, no. 6, pp. 1163–1175, Dec. 2006, doi: 10.1016/j.eururo.2006.06.025.

[19] O. Akin, E. Sala, C. S. Moskowitz, K. Kuroiwa, N. M. Ishill, D. Pucar, P. T. Scardino, and H. Hricak, "Transition zone prostate cancers: Features, detection, localization, and staging at endorectal MR imaging," *Radiology*, vol. 239, no. 3, pp. 784–792, Jun. 2006, doi: 10.1148/radiol.2392050949.

[20] J. O. Barentsz, J. Richenberg, R. Clements, P. Choyke, S. Verma, G. Villeirs, O. Rouviere, V. Logager, and J. J. Fütterer, "ESUR prostate MR guidelines 2012," *Eur. Radiol.*, vol. 22, no. 4, pp. 746–757, Apr. 2012, doi: 10.1007/s00330-011-2377-y.

[21] B. Zelhof, M. Pickles, G. Liney, P. Gibbs, G. Rodrigues, S. Kraus, and L. Turnbull, "Correlation of diffusion-weighted magnetic resonance data with cellularity in prostate cancer," *BJU Int.*, vol. 103, no. 7, pp. 883–888, Apr. 2009, doi: 10.1111/j.1464-410X.2008.08130.x.

[22] M. A. Jacobs, R. Ouwerkerk, K. Petrowski, and K. J. Macura, "Diffusion-weighted imaging with apparent diffusion coefficient mapping and spectroscopy in prostate cancer," *Topics Magn. Reson. Imag.*, vol. 19, no. 6, pp. 261–272, Dec. 2008, doi: 10.1097/RMR.0b013e3181aa6b50.

[23] L. Xu, G. Zhang, B. Shi, Y. Liu, T. Zou, W. Yan, Y. Xiao, H. Xue, F. Feng, J. Lei, Z. Jin, and H. Sun, "Comparison of biparametric and multiparametric MRI in the diagnosis of prostate cancer," *Cancer Imag.*, vol. 19, no. 1, p. 90, Dec. 2019, doi: 10.1186/s40644-019-0274-9.

[24] C. K. Kuhl, N. Bruhn, N. Krämer, S. Nebelung, A. Heidenreich, and S. Schrading, "Abbreviated biparametric prostate MR imaging in men with elevated prostate-specific antigen," *Radiology*, vol. 285, no. 2, pp. 493–505, Nov. 2017, doi: 10.1148/radiol.2017170129.

[25] M. Havaei, A. Davy, D. Warde-Farley, A. Biard, A. Courville, and Y. Bengio, "Brain tumor segmentation with deep neural networks," *Med. Image Anal.*, vol. 35, pp. 18–31, Jan. 2017, doi: 10.1016/j.media.2016.05.004.

[26] J. Dai, H. Qi, Y. Xiong, Y. Li, G. Zhang, H. Hu, and Y. Wei, "Deformable convolutional networks," in *Proc. IEEE Int. Conf. Comput. Vis. (ICCV)*, Venice, Italy, Oct. 2017, pp. 764–773.

[27] X. Zhu, H. Hu, S. Lin, and J. Dai, "Deformable ConvNets V2: More deformable, better results," in *Proc. IEEE/CVF Conf. Comput. Vis. Pattern Recognit. (CVPR)*, Long Beach, CA, USA, Jun. 2019, pp. 16–20.

[28] R. Toth and A. Madabhushi, "Multifeature landmark-free active appearance models: Application to prostate MRI segmentation," *IEEE Trans. Med. Imag.*, vol. 31, no. 8, pp. 1638–1650, Aug. 2012, doi: 10.1109/TMI.2012.2201498.

[29] W. Qiu, J. Yuan, E. Ukwatta, Y. Sun, M. Rajchl, and A. Fenster, "Dual optimization based prostate zonal segmentation in 3D MR images," *Med. Image Anal.*, vol. 18, no. 4, pp. 660–673, May 2014, doi: 10.1016/j.media.2014.02.009.

[30] Y. Zheng and D. Comaniciu, *Marginal Space Learning for Medical Image Analysis: Efficient Detection and Segmentation of Anatomical Structures*. New York, NY, USA: Springer, 2014. [Online]. Available: http://lib.myilibrary.com/detail.asp?id=635030

[31] N. Makni, A. Iancu, O. Colot, P. Puech, S. Mordon, and N. Betrouni, "Zonal segmentation of prostate using multispectral magnetic resonance images," *Med. Phys.*, vol. 38, no. 11, pp. 6093–6105, Oct. 2011, doi: 10.1118/1.3651610.

[32] G. Litjens, O. Debats, W. van de Ven, N. Karssemeijer, and H. Huisman, "A pattern recognition approach to zonal segmentation of the prostate on MRI," in *Proc. Int. Conf. Med. Image Comput. Comput.-Assist. Intervent.*, vol. 15, no. 2, 2012, pp. 413–420, doi: 10.1007/978-3-642-33418-4_51.

[33] S. Martin, J. Troccaz, and V. Daanen, "Automated segmentation of the prostate in 3D MR images using a probabilistic atlas and a spatially constrained deformable model," *Med. Phys.*, vol. 37, no. 4, pp. 1579–1590, Mar. 2010, doi: 10.1118/1.3315367.

[34] O. Chilali, P. Puech, S. Lakroum, M. Diaf, S. Mordon, and N. Betrouni, "Gland and zonal segmentation of prostate on T2W MR images," *J. Digit. Imag.*, vol. 29, no. 6, pp. 730–736, Dec. 2016, doi: 10.1007/s10278-016-9890-0.

[35] H. Jia, Y. Xia, Y. Song, W. Cai, M. Fulham, and D. D. Feng, "Atlas registration and ensemble deep convolutional neural network-based prostate segmentation using magnetic resonance imaging," *Neurocomputing*, vol. 275, pp. 1358–1369, Jan. 2018, doi: 10.1016/j.neucom.2017.09.084.

[36] R. Cheng, H. R. Roth, N. Lay, L. Lu, and B. Turkbey, "Automatic magnetic resonance prostate segmentation by deep learning with holistically nested networks," *J. Med. Imag.*, vol. 4, no. 4, p. 41302, 2017, doi: 10.1117/1.JMI.4.4.041302.

[37] Z. Tian, L. Liu, Z. Zhang, and B. Fei, "PSNet: Prostate segmentation on MRI based on a convolutional neural network," *J. Med. Imag.*, vol. 5, no. 2, p. 21208, 2018, doi: 10.1117/1.JMI.5.2.021208.

[38] D. Karimi, G. Samei, C. Kesch, G. Nir, and S. E. Salcudean, "Prostate segmentation in MRI using a convolutional neural network architecture and training strategy based on statistical shape models," *Int. J. Comput. Assist. Radiol. Surg.*, vol. 13, no. 8, pp. 1211–1219, Aug. 2018, doi: 10.1007/s11548-018-1785-8.

[39] Y. Guo, Y. Gao, and D. Shen, "Deformable MR prostate segmentation via deep feature learning and sparse patch matching," *IEEE Trans. Med. Imag.*, vol. 35, no. 4, pp. 1077–1089, Apr. 2016, doi: 10.1109/TMI.2015.2508280.

[40] Y. Weng, T. Zhou, Y. Li, and X. Qiu, "NAS-Unet: Neural architecture search for medical image segmentation," *IEEE Access*, vol. 7, pp. 44247–44257, 2019, doi: 10.1109/ACCESS.2019.2908991.

[41] Q. Zhu, B. Du, B. Turkbey, P. L. Choyke, and P. Yan, "Deeply-supervised CNN for prostate segmentation," in *Proc. Int. Joint Conf. Neural Netw. (IJCNN)*, Anchorage, AK, USA, May 2017, pp. 178–184.

[42] F. Milletari, N. Navab, and S.-A. Ahmadi, "V-Net: Fully convolutional neural networks for volumetric medical image segmentation," in *Proc. 4th Int. Conf. 3D Vis. (3DV)*, Stanford, CA, USA, 2016, pp. 565–571.

[43] F. Zabihollahy, N. Schieda, S. K. Jeyaraj, and E. Ukwatta, "Automated segmentation of prostate zonal anatomy on T2-weighted (T2W) and apparent diffusion coefficient (ADC) map MR images using U-Nets," *Med. Phys.*, vol. 46, pp. 3078–3090, Jul. 2019, doi: 10.1002/mp.13550.

[44] Y. Zhu, R. Wei, G. Gao, L. Ding, X. Zhang, X. Wang, and J. Zhang, "Fully automatic segmentation on prostate MR images based on cascaded fully convolution network," *J. Magn. Reson. Imag.*, vol. 49, no. 4, pp. 1149–1156, Apr. 2019, doi: 10.1002/jmri.26337.

[45] Y. Qian, Z. Zhang, and B. Wang, "ProCDet: A new method for prostate cancer detection based on MR images," *IEEE Access*, vol. 9, pp. 143495–143505, 2021, doi: 10.1109/ACCESS.2021.3114733.

[46] Y. Qian, "ProSegNet: A new network of prostate segmentation based on MR images," *IEEE Access*, vol. 9, pp. 106293–106302, 2021, doi: 10.1109/ACCESS.2021.3096665.

[47] D. Ciresan, U. Meier, and J. Schmidhuber, "Multi-column deep neural networks for image classification," in *Proc. IEEE Conf. Comput. Vis. Pattern Recognit. (CVPR)*, Providence, RI, USA, Jun. 2012, pp. 3642–3649.

[48] X. Yuan, Z. Feng, M. Norton, and X. Li, "Generalized batch normalization: Towards accelerating deep neural networks," in *Proc. AAAI Conf. Artif. Intell.*, vol. 33, no. 1, pp. 1682–1689, Jul. 2018.

[49] K. He, X. Zhang, S. Ren, and J. Sun, "Deep residual learning for image recognition," in *Proc. IEEE Conf. Comput. Vis. Pattern Recognit. (CVPR)*, Las Vegas, NV, USA, Jun. 2016, pp. 770–778.

[50] D. E. Rumelhart and J. L. McClelland, *Parallel Distributed Processing: Explorations in the Microstructure of Cognition*. Cambridge, MA, USA: MIT Press, 1986. [Online]. Available: http://ieeexplore.ieee.org/servlet/opac?bknumber=6276825

[51] X. Huang, B. Zhang, X. Zhang, M. Tang, Q. Miao, T. Li, and G. Jia, "Application of U-Net based multiparameter magnetic resonance image fusion in the diagnosis of prostate cancer," *IEEE Access*, vol. 9, pp. 33756–33768, 2021, doi: 10.1109/ACCESS.2021.3061078.

[52] N. Aldoj, F. Biavati, F. Michallek, S. Stober, and M. Dewey, "Automatic prostate and prostate zones segmentation of magnetic resonance images using DenseNet-like U-net," *Sci. Rep.*, vol. 10, no. 1, p. 14315, Aug. 2020, doi: 10.1038/s41598-020-71080-0.

[53] A. Machireddy, N. Meermeier, F. Coakley, and X. Song, "Malignancy detection in prostate multi-parametric MR images using U-Net with attention," in *Proc. 42nd Annu. Int. Conf. IEEE Eng. Med. Biol. Soc. (EMBC)*, Jul. 2020, pp. 1520–1523, doi: 10.1109/EMBC44109.2020.9176050.

[54] Y. Jin, G. Yang, Y. Fang, R. Li, X. Xu, Y. Liu, and X. Lai, "3D PBV-Net: An automated prostate MRI data segmentation method," *Comput. Biol. Med.*, vol. 128, Jan. 2021, Art. no. 104160, doi: 10.1016/j.compbiomed.2020.104160.

[55] B. Wang, Y. Lei, S. Tian, T. Wang, Y. Liu, P. Patel, A. B. Jani, H. Mao, W. J. Curran, T. Liu, and X. Yang, "Deeply supervised 3D fully convolutional networks with group dilated convolution for automatic MRI prostate segmentation," *Med. Phys.*, vol. 46, no. 4, pp. 1707–1718, Apr. 2019, doi: 10.1002/mp.13416.

[56] J. He, X. Li, N. Liu, and S. Zhan, "Conditional generative adversarial networks with multi-scale discriminators for prostate MRI segmentation," *Neural Process. Lett.*, vol. 52, no. 2, pp. 1251–1261, 2020, doi: 10.1007/s11063-020-10303-x.

XUNAN HUANG received the Ph.D. degree from the School of Computer Science and Technology, Xidian University, in 2021. Since 2022, he has been a Lecturer with the Air Traffic Control and Navigation College, Air Force Engineering University, Xi'an, Shaanxi, China. His current research interests include medical image processing, pattern recognition, and deep learning.

BO PANG received the M.S. degree from Defence Science University, China, in 2016. Since 2020, he has been a Lecturer with the Air Traffic Control and Navigation College, Air Force Engineering University, Xi'an, Shaanxi, China. His current research interests include intelligent image processing, pattern recognition, and deep learning.

TAO ZHANG is currently an Associate Professor and a Supervisor of M.S. students with the Air Traffic Control and Navigation College, Air Force Engineering University. His research interests include computer vision, machine learning, and big data.

YING WANG is currently a Professor and a Supervisor of M.S. students with the Air Traffic Control and Navigation College, Air Force Engineering University. Her current research interests include computer simulation and image processing.

GUANG JIA received the B.S. degree in theoretical physics from Lanzhou University, in 1997, and the Ph.D. degree in biophysics from The Ohio State University, Columbus, OH, USA, in 2006. He was a Postdoctoral Researcher (2006–2008), an Instructor (2008–2011), and an Assistant Professor (2011–2013) with the Department of Radiology, The Ohio State University. From 2013 to 2016, he was an Associate Professor with the Department of Physics, Louisiana State University, Baton Rouge, LA, USA. Since 2017, he has been a Professor with the School of Computer Science and Technology, Xidian University, Xi'an, Shaanxi, China. He is the author of 50 articles and ten inventions. His research interests include diagnostic medical physics and AI-based medical image processing. He was a recipient of the Radiological Society of North America Research Trainee Prize, in 2008, the American Urological Association Foundation Outstanding Graduate Scholar Award, in 2011, and the American College of Radiology Imaging Network Young Investigator Award, in 2012.

YONGLIN LI received the Ph.D. degree in aerospace science and technology from the School of Aeronautical Engineering, Air Force Engineering University, in 2011. He is a postdoctoral researcher in control science and technology. He is currently an Associate Professor with the School of Air Traffic Control and Navigation, Air Force Engineering University. His research interest includes intelligent task planning.

● ● ●